Interfaces between crystalline Si and amorphous B: interfacial interactions and charge barriers

Piet Xiaowen Fang,[1,2] Stoyan Nihtianov,[1] Paolo Sberna,[1] and Changming Fang[3,*]

[1] *Electronic Instrumentation Lab, Faculty of Electrical Engineering, Mathematics and Computer Science, TU Delft, Mekelweg 4, 2628 CD Delft, The Netherlands.*
[2] *High Field Magnet Laboratory (HFML-EMFL), Radboud University, Toernooiveld 7, 6525 ED Nijmegen, The Netherlands*
[3] *BCAST, Brunel University London, Uxbridge, Middlesex, UB8 3PH, UK.*

(Dated: January 15, 2021)

The recently found crystalline Silicon-amorphous Boron (c-Si/a-B) heterojunction has been successfully applied in the detection of short-wave UV photons. These detectors play a decisive role in the progress of nanoelectronics fabrication. The c-Si/a-B heterojunction could not be explained using the existing 'instrumentarium' in semiconductor physics. We investigated the c-Si/a-B interfaces using *ab initio* molecular dynamics simulations. The simulations reveal atomic ordering of the a-B atoms adjacent to both the Si{0 0 1} and Si{1 1 1} substrates. Charge transfer occurs from the interfacial Si to B, thereby forming Si^+/B^- charge barriers, which induce an electric field in the nearby regions. The obtained information here is helpful in furthering our understanding of the physics behind the c-Si/a-B junctions, as well as driving the development of a new 'instrumentatrium' in solid state physics.

I. INTRODUCTION

Progress in nanoelectronics fabrication is at present highly dependent on advances in UV photolithography techniques. This in turn has lead to a demand for high-performance shortwave UV detectors (for wavelengths between 1-200 nm) [1–5]. These UV photons have very shallow penetration depths; junctions with ultra-thin deposition layers are therefore a requirement. Si-based junctions (or photodiodes) are good candidates for this application due to both their low cost and the availability of well-established production techniques.

A promising candidate is the crystalline Silicon-amorphous Boron (c-Si/a-B) junction. The junction consists of a nanometer-thin (typically 1 to 5 nm) amorphous boron (a-B) layer on a crystalline silicon (c-Si) substrate. This junction is produced by deposition of amorphous B on Si wafers via decomposition of borane at an elevated temperature, through a technique referred to as the PureB process [1–4, 6–9]. While this technology has already been successfully applied in the design and creation of new UV detectors [4], there is a lack of profound understanding concerning the exact mechanism behind this new type of junction. The classic theory for semiconductor devices is based on descriptions for either doped Si^+ on Si^- (e.g. B-doped Si^+ on P-doped Si^-, p-n junctions), or Si-metal interfaces (Schottky diode) [10–12] and proves to be insufficient to describe this class of junction [13].

Currently, experiments have primarily been focused on studying the PureB processes as well as the optoelectrical properties of the produced c-Si/a-B junctions [5, 14–16]. In more recent studies the local structure and composition of the interface were investigated using high resolution electron microscopy (HR-EM) techniques [7, 16, 17]. The HR-EM images revealed the formation of mixed B-Si layers for samples prepared at high temperature (~700 °C), whereas little B-Si mixing was observed for samples with a lower preparation temperature (~400 °C) [1–3, 7, 18, 19].

On the theoretical side, parameter-free first-principles approaches are very useful to get insight into the mechanism of heterojunctions. In particular, *ab initio* molecular dynamics (AIMD) simulation techniques have been successfully applied before to investigate the interfaces between crystalline Si and amorphous silicon oxide (c-Si/a-SiO_2) [20] as well as crystalline Si and amorphous silicon nitrides (c-Si/a-Si_3N_{4-x}) [21–23]. First-principles methods were also used to study the bulk properties of silicon, its clean [24] and hydrogen passivated surfaces [25], borane radicals deposited on the surfaces [6, 8, 26, 27] and some Si-metal (Schottky) barriers [12]. Recently, we also performed AIMD simulations on the Si{1 0 0}/a-B interface to aid experimental observations [7]. However, details on the local chemical bonding and electronic properties at the c-Si/a-B interfaces are sparse.

Within the semiconductor industry Si{0 0 1} is used predominantly in the production of electronic devices. However, Si{1 1 1} wafers are available commercially as well. The Si{1 1 1} atoms exhibit different symmetry and chemical properties. The atoms at the pristine Si{0 0 1} surface lose two Si neighbors when considering coordination numbers, whereas an interfacial Si atom at the pristine Si{1 1 1} surface loses only one neighbor.

In this work we investigate the formation of interfaces between a-B and c-Si in both the {0 0 1} and the Si{1 1 1} orientations using AIMD simulation techniques. The simulations produce atomically sharp Si-B interfaces and further analysis reveals charge transfer at the interfaces. We consider this mechanism to play a key role in the

* Changming.Fang@brunel.ac.uk

Table I: Input parameters of the supercells used for AIMD simulations of the c-Si/a-B interfaces.

Interface	Lattice	Unit params.		No. of atoms		Bonding of pristine interface
		a (Å)	c (Å)	N_{Si}	N_{B}	
Si{0 0 1}/a-B_{I}	Tetragonal	16.45	19.18	144	300	Each Si_{surf} loses two neighbors
Si{0 0 1}/a-B_{II}	Tetragonal	16.45	27.44	144	600	
Si{1 1 1}/a-B_{I}	Hexagonal	15.51	26.65	192	300	Each Si_{surf} loses one neighbor
Si{1 1 1}/a-B_{II}	Hexagonal	15.51	40.30	192	600	

electronic properties of the c-Si/a-B junction. The information obtained here sheds some light on the formation of the c-Si/a-B junctions, and we believe it will be useful for a better understanding on the formation of other hetero-junctions as well.

II. METHODS

The AIMD approach employs periodic boundary conditions (PBC). For the Si{0 0 1}/a-B systems, we utilized a tetragonal supercell with $a = b = 3a_0$ (with a_0 the lattice parameter of Si at the simulation temperature [28, 29]). For the Si{1 1 1}/a-B system, a hexagonal lattice was used with the in-plane lattice parameter $a = b = 2\sqrt{2}a_0$. The length of the c-axis was determined by the volume of the a-B atoms and the thickness of the Si part [28, 29]). Different amounts of amorphous boron atoms were also used to avoid accidental cases. The lattice parameters and numbers of atoms used as inputs are listed in Table I. These supercells are required provide statistically meaningful results.

Amorphous B (a-B) samples were first heated at 4000 K (T_{melt} for B is 2348 K) for 2000 steps (1.5 fs per step), or 3.0 ps in total, before cooling to the simulation temperature. The obtained samples and the Si slabs were then used to build in the interface systems. We used a two-step approach to simulate the interface systems.

We first performed simulations for the built systems with the Si atoms pinned in the substrates at 1000 K for about 1.5 ps. Then, we equilibrated the interface system with full relaxation of all atoms at a 1000 K and 700 K for another 3000 steps, respectively. The simulations show that this two-step approach avoid the risks of collective movements of atoms. We took samples at an internal time of about 0.1 ps after the system reached equilibrium (at about 2 ps simulation time). Finally, the obtained samples were relaxed to remove the internal forces [30, 31]. We also relaxed structures of amorphous B samples with different densities, which were then used to calculate the electronic structure.

In the current AIMD simulations, we employed a pseudo-potential plane-wave approach within the density-functional theory (DFT) [32, 33] within the first-principles code of the Vienna *Ab initio* Simulation Package (VASP). This code utilizes the projector augmented-wave (PAW) method [34, 35]. Moreover, it allows variable fractional occupation numbers and therefore works well for the semiconducting/metallic interfaces [32]. The AIMD simulation employs the finite-temperature density functional theory of the one-electron states, the exact energy minimization and calculation of the exact Hellmann-Feynman forces after each MD step using preconditioned conjugate techniques, and the Nosé dynamics for generating a canonical NVT ensemble [32, 33]. The exchange and correlation terms are described using the generalized gradient approximation (GGA) [36].

The atomic electronic configurations in pseudopotentials for B and Si are [He] $2s^2 2p^1$ and [Ne] $3s^2 3p^2$ respectively. For structural optimizations, we used cut-off energies of 400.0 eV for the wave functions and 550.0 eV for the augmentation functions. These energies are higher than the corresponding default values ($E_{\mathrm{cut}}/E_{\mathrm{aug}}$ = 318.6/535.3 eV and 245.3/322.1 eV resp. for B and Si). The electronic wave functions were sampled on dense grids, e.g. a $24 \times 24 \times 24$ (413 k-points) and $30 \times 30 \times 30$ k-mesh (183 k-points) in the irreducible Brillouin zone (BZ) of the conventional cell for Si and the hexagonal cell of α-B, respectively [37].

For the AIMD simulations of the large supercells we used E_{cut} = 320 eV and simulated only the Γ-point in the BZs. The dynamics of amorphous-solid/crystal interfaces, molecular/surface reactions and low-dimensional structure are typically modeled using Γ-point sampling due to the lack of periodicity of the overall system [6, 30, 31, 38]. This helps in tuning the demand of computations to obtain reliable results to the capabilities of the computer cluster. Our prior simulations that tested different cut-off energies, ranging from 200.0 eV to 400.0 eV demonstrated that the settings are reasonable

III. RESULTS

First-principles structure optimizations were then performed for the elemental solids using the settings mentioned above. The calculated lattice parameter for the cubic Si is 5.469 Å, which is slightly larger than the experimental value (5.4309 Å) [28]. Each Si atom is in tetragonal coordination with Si-Si bond-length of 2.37 Å. The calculations also produced lattice parameters for α-B which has a rhombohedral lattice. The calculated lattice parameters are a = 5.057 Å, α = 58.04°. These values agree with the experimental values, a = 5.06 Å,

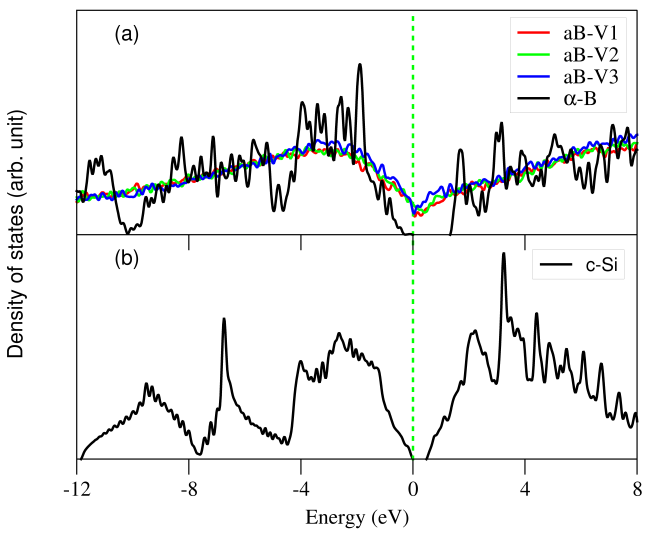

Figure 1: (Colors online) Total density of states of boron atoms of the crystalline α and amorphous phase (a) with different densities (b) and of crystalline Si. The Fermi level is given in green. In 1a, the density of a-B is represented by aB-V1, aB-V2 and aB-V3 with values of 2.44 g/cm^3, 2.35 g/cm^3, 2.08 g/cm^3 respectively.

$\alpha = 58.09°$ [29]. The boron atoms have 6 to 7 neighbors with interatomic distances ranging from 1.71 to 2.02 Å. Such overestimation of lattice parameters of crystals is not unusual for simulations using DFT-GGA [39]. The results for the elemental solids are therefore well in agreement with the experimental data found in literature with a deviation of <1%.

Furthermore, band structure calculations were performed for crystalline Si and α-B. The calculations predict that Si is an indirect semiconductor: The top of the valence bands for both crystals are at the Γ point and the bottom of the conduction band is at (0.4167, 0.4167, 0.0) in the Brillouin zones. The calculated indirect gap for Si is 0.61 eV using this approach. The calculated energy gap is noticeably smaller than the experimental value (1.17 eV) [39]. The calculations revealed a semiconducting nature for the crystalline boron when analyzing the density of states as shown in Fig. 1. The calculated band gap is 1.50 eV which is also smaller than the experimental value (2.0 eV) from resistivity measurements [40]. An underestimation of band gaps for semiconducting crystals is not unusual for the standard density functional calculations including the GGA method [39, 41].

Fig. 1 also includes the total density of states (DOS) for the a-B samples with different densities. The frame of the DOS curves of a-B and the crystalline phase are similar with the exception of a band gap for the latter. The calculated Fermi level of amorphous B is about 0.4 eV higher than the Fermi level of c-B. Correspondingly, the Fermi level of the calculated DOS curves is set at zero eV. The Fermi level of a-B is located in the valleys of the DOS curve. Analysis shows that the states around the Fermi level are strongly localized. This is due to local structural distortions/defects, a lack of long-range ordering and strong interatomic interaction in a-B.

A. Interface formation and local bonding at the interfaces

During the AIMD simulations the amorphous B atoms move towards the pinned Si substrates and correspondingly the total electron energies of the systems decreased rapidly within the first 1 ps, which was then followed by a steady decrease. There was also a change in energy due to relaxation of both the Si and the B atoms. The systems reached equilibrium after 1.0 ps with full relaxation.

Fig. 2 shows the snapshots of the relaxed c-Si/a-B interfaces and related typical local chemical bonding and Si coordination at the interfaces. The snapshots provide us with direct impressions of the local structure of the interfaces. Figs. 2a and 2d shows that for both interfaces the boron atoms away from the substrates remain disordered. The interfacing amorphous B atoms also remain well-separated from the Si substrates. There are a number of subtle differences between the two interfaces:

1. The spacing between the Si substrate to the amorphous B at the Si{1 1 1}/a-B interface is larger than for Si{0 0 1}/a-B;
2. The B atoms adjacent to Si{1 1 1} are positioned mainly on top of Si atoms;
3. The interfacial Si atoms at Si{0 0 1}/a-B have dominantly two B neighbors (Figs. 2b and 2c), whereas those at Si{1 1 1}/a-B have one B neighbors (Figs. 2e and 2f);
4. The density of boron atoms near the Si{0 0 1} substrate (Fig. 2a) appears higher than in the case of the Si{1 1 1} substrate (Fig. 2d).

These Si-B bonds were analyzed for ~20 samples per interface. The Si-B bond lengths are at most 2.28 Å, which is 10% longer than the average B-B (1.79 Å) and Si-Si bondlength (2.35 Å) in the elemental solids respectively when taking into account the exponential decay of bond strength on interatomic distance [42]. The results of this analysis are shown in Fig. 3.

From this analysis it was found that 88% of Si atoms at the Si{1 1 1}/a-B interface are coordinated by one B which together with the three Si-Si bonds satisfies the tetragonal coordination (sp^3 hybridization) [43]. Roughly 10% of the interfacial Si atoms coordinated with two B atoms. The analysis also revealed few cases where a B atom is bonded to a Si at the subsurface Si layer. This is likely due to the kinetic factor present during the molecular dynamics simulations.

The Si coordination of Si at the Si{0 0 1}/a-B interfaces is more complex (Figs. 2 and 3). The majority of the Si-atoms at the Si{0 0 1}/a-B interface have two B neighbors (57%). A certain 29% of the interfacial Si atoms have three B neighbors, a further 9% of the inter-

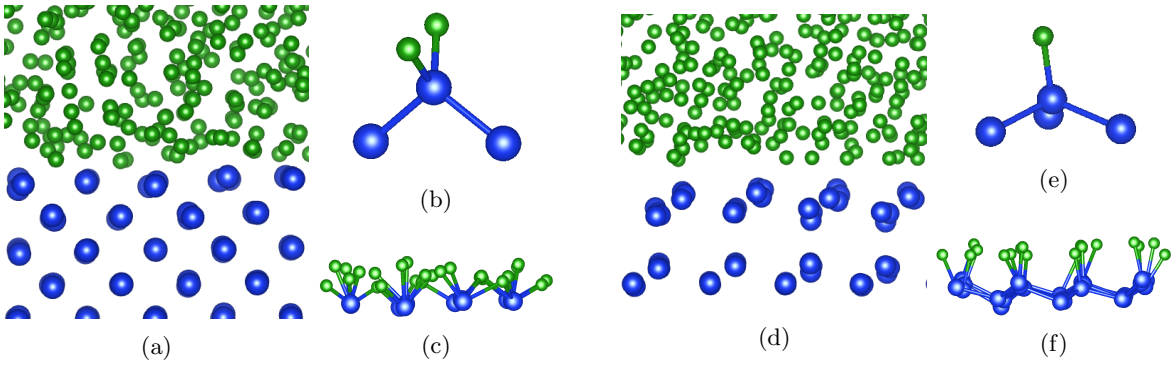

Figure 2: (Color online) Snapshots of simulated a-B/Si{0 0 1} (a) and a-B/Si{1 1 1} (d) interfaces. Also given are examples of Si coordination of an interfacial Si and local chemical bonding at the a-B/Si{0 0 1} (b, c) and the a-B/Si{1 1 1} (e, f) interface, respectively. The small green spheres and the larger blue spheres represent B and Si respectively.

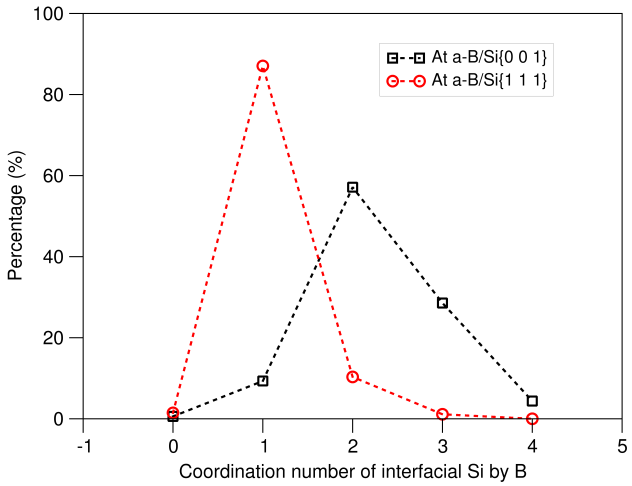

Figure 3: (Color online) Distribution of the number of closest nearest neighboring (CNN) B atoms for interfacial Si atoms at the Si{0 0 1}/a-B (red circles) and Si{1 1 1}/a-B (black squares) interfaces.

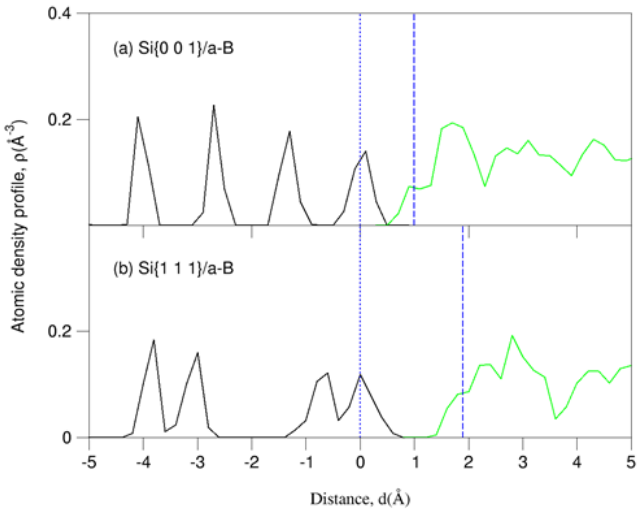

Figure 4: (Color online) Atomic density profiles of the (above) Si{0 0 1}/a-B and (below) Si{1 1 1}/a-B interface equilibrated and annealed interface at 0 K, where the black lines represent $\rho(z)$ for Si atoms and the green for B atoms. The broken blue lines show the first boron peaks and the dotted blue line represents the outermost Si layer.

facial Si have only one B neighbor and finally 4% of the surface Si at atoms have four B neighbors. The larger variety of Si coordination at the Si{0 0 1}/a-B interfaces originates from the reduced constraint from the Si substrates as each surficial Si is bonded to only two Si atoms at the subsurface. The different local Si-B bonding indicate variation in B arrangements at the interfaces, as shown in Figs. 2b, 2c, 2e and 2f. This corresponds to a variation in the B density along the direction perpendicular to the substrates (layering). The unusual steric hindrance and local Si-B bonding at Si{1 1 1}/a-B indicate higher energy barriers for B diffusion into Si as compared with that at the Si{0 0 1}/a-B. This is in line with the previous experimental results that at high temperature (~1073 K) the B diffusion rate at the Si{0 0 1} wafers is notably higher than that at Si{1 1 1} during the molecular layer doping process [44]. To assess the layering phenomenon at the interfaces, we introduce the atomic density profile. It is defined as follows [31, 45]:

$$\rho(z) = \frac{< N_z(t) >}{L_x L_y \delta z}, \quad (1)$$

where L_x and L_y are the in-plane x and y dimensions of the cell respectively with z the dimension perpendicular to the interface, δz is the bin width and $N_z(t)$ is the number of atoms between $z-(\delta z/2)$ and $z+(\delta z/2)$ at time t. $< N_z(t) >$ is the time-averaged number of atoms in the duration. The atomic density profiles for the c-Si/a-

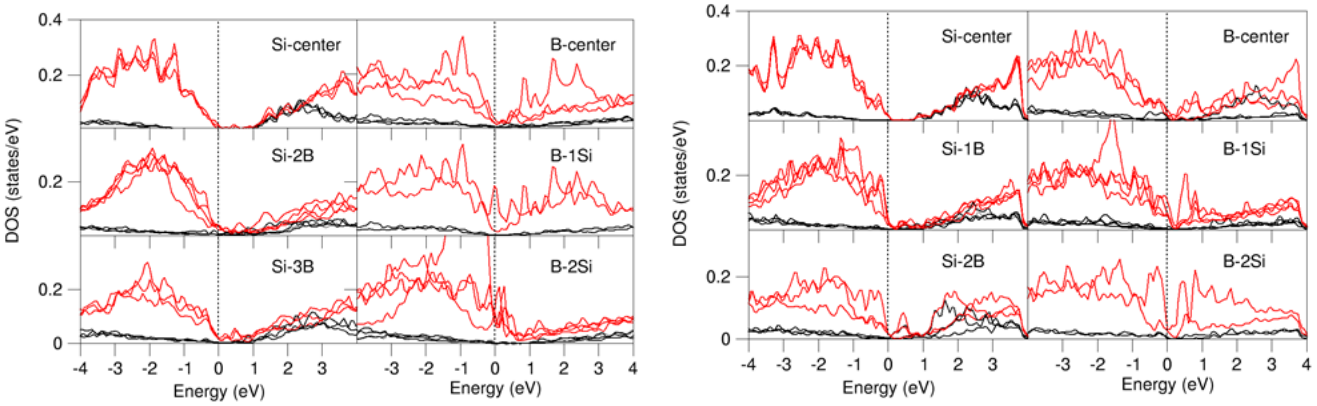

(a) (b)

Figure 5: (Color online) Partial density of states (pDOS) of the Si 3s and 3p states as well as the B 2s and 2p states at the Si{0 0 1}/a-B (a) and Si{1 1 1}/a-B (b) interfaces around the Fermi level (0 eV). The black and red curves represent Si/B 3s/2s characters and 3p/2p states respectively. The dotted line at zero eV represents the Fermi level.

B interfaces were analyzed for the relaxed configurations. The results are plotted in Fig. 4.

Our calculations for the interfaces of different a-B thicknesses also showed that there is no notable difference between the two density profiles. The atomic density profiles confirm our impression from the snapshots (Fig. 2). The Si substrates are well-separated from the amorphous B. The single Si peaks in the Si{0 0 1} substrate and the double Si-Si peaks in the Si{1 1 1} substrates can easily be recognized. The statistics show a clear gap between the substrates and the amorphous boron. The a-B atoms near the substrates exhibit density variations.

The analysis also shows a larger spacing (1.9 Å) at the Si{1 1 1}/a-B interfaces compared to Si{0 0 1}/a-B (1.1 Å). Moreover, the amorphous B adjacent to the Si substrates form peaks. The amorphous B form a broad peak centered at about 1.7 Å (Peak 2) and a valley at about 2.3 Å. A second B peak is centered at 2.3 Å (Peak 2) and a third peak is seen at 2.8 Å with a valley at 3.6 Å. Such unevenness and fluctuation in the B densities comes from the chemical interaction at the Si-B interfaces.

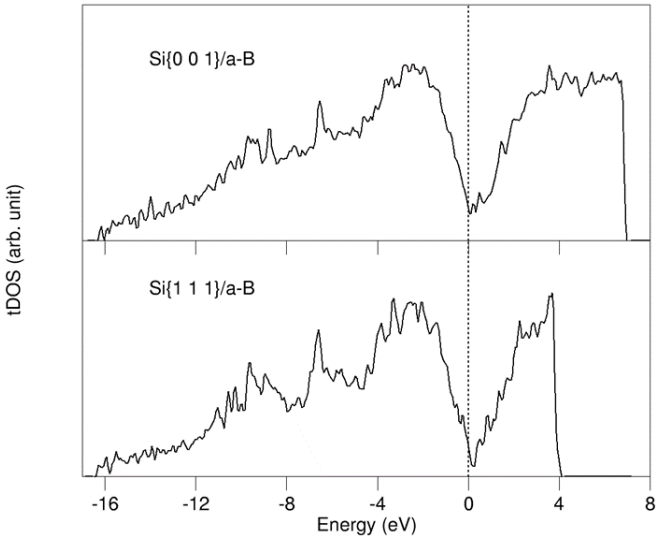

Figure 6: Total DOS of the Si{0 0 1}/a-B (top) and Si{1 1 1}/a-B interfaces. The dotted line at zero eV represents the Fermi level.

B. Electronic properties of the c-Si/a-B interfaces

Band structure calculations were also performed to study the interfacial interaction and related electronic properties. The partial density of states (pDOS) and total DOS (tDOS) of selected Si and B atoms both at the substrate/amorphous B as well as at the interfaces with typical Si-B bonds are shown in Figs. 5 and 6 respectively. The dispersion curves around the Fermi level in the ab-planes for the two interfaces were also plotted in Fig. 7.

At both interfaces, all the Si and B atoms have similar electronic structure with a valence band and a conduction bands as shown in Fig. 5. Both Si/B s and p states are all over the entire valence and conduction bands. The states of s-character dominate the lower part of the valence band and extend to the conduction band, whereas the p-states dominate the upper part of the valeunce band and the conduction band. This corresponds to the sp hybridization in crystalline Si and amorphous B parts. Fig. 5 also shows that the Si in both substrates have an energy gap of about 0.7 eV. This band gap is close to the calculated band gap of bulk Si. The Fermi level is also at the top of valence band for the interfacial Si atoms. There are unoccupied defect states at the forbidden gap of the interfacial Si atoms, as shown in Fig. 7, corresponding to electron loss from Si to its neighboring B atoms. These results indicate a valence-band off-set

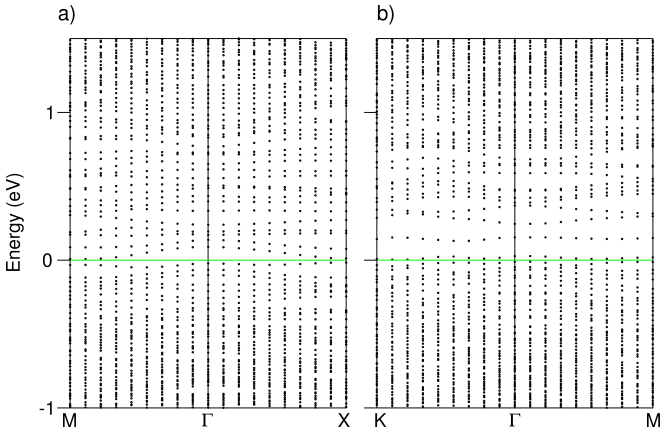

Figure 7: Dispersion curves around the Fermi levels (green lines at zero eV) for the (a) Si{0 0 1}/a-B and (b) Si{1 1 1}/a-B interfaces in the ab-planes.

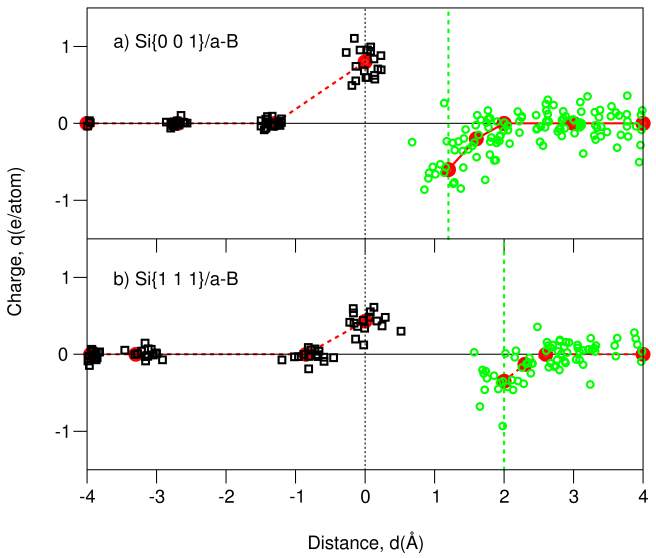

Figure 8: (Color online) Charges at the c-Si/a-B interfaces. The red dots, black squares and green circles represent the average charge values of each layer, the Si sites and the B sites respectively. The black dotted vertical line indicate the peak of the outermost Si, while the dotted green one represent the first peak of B atoms.

for Si atoms near the interfaces.

The tDOS curves provide information on the Si substrates, the amorphous B and interfaces Si and B atoms (Fig. 6). The shapes of the two curves are similar to each other: The valence bands start at around -16.3 eV and the density increases with energy up until roughly 2 eV below the Fermi level. Then the density of states decreases as energy increases. There is a pseudo-gap around the Fermi level at both interface systems. This gap is largely due to Si (see Fig. 5). The tDOS above the gap increases with energy. The states at the energy gap originate from the interfacial Si/B and the amorphous B, as detailed in Fig. 5. The dispersion curves show localized bands ranging from the Fermi level to about 0.7 eV (Fig. 7), originating from the a-B and the surficial Si/B atoms.

The valence band of a-B starts at about -16.3 eV for both interfaces. The DOS of the Si in the substrates starts at about -12.0 eV in Fig. 6. There are also some states between -16.3 eV to -12.0 eV for the interfacial Si atoms. This comes from the Si-B hybridization at the interfaces. The p-states are suppressed and evenly distributed between -4.0 to -1.0 eV for the Si in the substrate, whereas they are dominant at approximately -3.0 to 0.0 eV for the interfacial Si, especially at the Si{0 0 1}/a-B interface. At the Si{0 0 1}/a-B interface, the interfacial B atom has a unique DOS of the 2p states with high density near the Fermi level, whereas the 2p states of an a-B atom are distributed from -5.0 to 0.0 eV. There is an energy gap for the Si atoms in the substrates at both systems. The DOS above the Fermi level for the interfacial B atoms is weak while there are 2p states up to 3.5 V for a-B. This unusually high density of 2p states for the interfacial B indicates extra band-filling with charge from the nearby Si atoms. It is also notable that the interfacial effect on the electronic properties at the Si{0 0 1}/a-B is more pronounced that that at the Si{1 1 1}/a-B interface.

C. Charge transfer and charge barrier at the c-Si/a-B interfaces

The charge density between atoms/ions as well as the charge transfer at this interface provide a more direct message to understand the interfacial interaction. Bader employed a unique way to define the shape and volume and electrons of an atom in solid using the electron density distributions from first-principles calculations [46]. This approach has been successfully applied to various systems [47, 48]. Fig. 8 shows the charges at the atomic sites at the two studied interface systems using the Bader charge analysis approach. The Si and a-B atoms away from the interfacial layers are electronically neutral. Charge transfer only occurs from interfacial Si atoms to interfacial B atoms. The average amount of charge transfer is calculated to be 0.75 e/Si for Si{0 0 1}/a-B. In the case of Si{1 1 1}/a-B this is 0.40 e/Si. From these values we estimate the charge densities at the interfaces. The atomic density of Si{0 0 1} is 6.78×10^{18} m^{-2}, which is the same at the Si{1 1 1} surface when only the top Si atoms are counted as shown in Fig. 8. The charge density then is 4.7×10^{18} em^{-2} or 0.815 Cm^{-2} ($e = -1.602 \times 10^{-19}$ C) for Si{0 0 1}/a-B and 2.7×10^{18} em^{-2} or 0.435 Cm^{-2} for {1 1 1}/a-B.

These values correspond to the number of Si-B bonds at the interfaces: Most of the interfacial Si atoms at Si{1 1 1}/a-B have one B neighbor, whereas most interfacial Si atoms at Si{0 0 1}/a-B have on average more than two B neighbors, referring back to Fig. 3. The amount of charge at the interface (0.4 e/Si for Si{0 0 1}/a-B and

0.75 e/Si for Si{1 1 1}/a-B) is smaller compared to the values obtained using an ionic model (1.0 e/Si and 2.0 e/Si respectively, according to the averaged coordination numbers of Si by B (Fig.3)). This is an indication of the ionic and covalent dual nature of the interfacial Si-B bonding. Such strong interfacial bonding also indicates strong mechnical properties of the interfaces.

The AIMD simulations revealed the formation of sharp c-Si/a-B interfaces. Charge transfer from the interfacial Si to B takes place at atomic level, forming Si^{+q}/B^{-q} dipole layers at the c-Si/a-B interfaces. This charge transfer originates from a difference between the electronegativity of Si (1.90 in Pauling scale) and B (2.04). In the Si-B bonds electrons move from Si^{+} to B^{-} freely. Outside of the dipole plane, the Si-B dipoles induce a positive/negative electric field in the nearby c-Si/a-B region. The potential energy of linear dipoles decreases with r^{-3} or even faster) [49, 50]. The formed electric fields at the c-Si/a-B interfaces bans/permits hole-/electron-carriers from passing through entering from the Si/B side. This is what is responsible for the rectifying and the electronic properties of the diodes.

IV. DISCUSSION

A. Intrinsic electronic properties of a-B

Elemental boron exhibits a large number of allotropes, most of them containing over a hundred atoms in the unit cell [51–53]. Theoretical studies based on quantum-mechanical approaches showed that several boron phases, including the α-rhombohedral phase (B_{12}) are stable at ambient conditions [53]. Structurally, the B phases of high stability at ambient conditions are composed of B_{12} octahedral building blocks. We have calculated the electronic structure of the crystalline α-rhombohedral phase as shown in Fig. 1. The calculated energy gap is 1.5 eV which is smaller than the experimental value (2.0 eV) from resistivity measurements [40].

Amorphous boron (a-B) has been also investigated intensively before. The studies showed that there is no long range ordering in a-B. However, a short-range ordering is present in a-B. The overall structure of a-B also contains B_{12} octahedra albeit in a distorted form [54, 55]. When compared to amorphous Si [56], the electronic structure of a-B contains higher concentrations of tailed states and defects in the forbidden gap due to the higher concentration of structural distortions and defects.

This is confirmed by our band structure calculations as shown in Fig. 1. The Fermi level clearly falls in the valley in the tDOS curve. There still is a considerable density around Fermi level, indicating a metallic nature. The calculations also showed that the variation of a-B density from 2.43 g/cm^3 (similar to that of solid B [29]) to 2.08 g/cm^3 (close to that of liquid B [29]) has little influence on the electronic properties as shown in Fig. 1. However, the lack of long-range ordering (LRO) indicates that these states are localized. Experiments provided a large variance of energy gaps for a-B depending on preparation conditions and impurities as reviewed in a recent paper [57]. For deposited a-B samples, the experimental value of the energy gap is 0.5 to 0.75 eV [58–60]. The electrical transport properties measurements showed that the dominant charge carriers in a-B are holes [61, 62]. Experiments also showed that impurities, including hydrogen and oxygen, may play a role on the band gap opening and electrical properties [57, 63–65].

Overall, based on our AIMD simulations and band structure calculations, we conclude that a-B is intrinsically a 'bad' metal which consists of localized states. This indicates hopping mechanism for electrical transport, which corresponds to the high resistance of a-B [57, 59–62]. This influences the electrical properties and the band offset at the c-Si/a-B interfaces. This is somewhat different from the experiments. Such discrepancy comes from the widely existing impurities, such as H and O and partial crystallization in prepared samples. The widely existing impurities, such as H, may cure the defects and related defect states and open an band gap in amorphous materials [56, 66]. The charge carriers in pure a-B originating from the localized defect states have large effective masses and hop under electrical fields. Another point is partial crystallization of amorphous B samples during annealing at high temperature. Due to this, further investigation is necessary to reconcile our theoretical results with experimental values.

B. Band offset at c-Si/a-B interfaces

The present study revealed formation of strong interfacial interaction at the c-Si/a-B interfaces. There is charge transfer from the interfacial Si to B, forming Si^{+}/B^{-} charge barriers, which induce positive/negative electric fields at the nearby Si/B regions. This is also an indicator for the strong mechanical properties of this heterojunction. The charge model is schematically shown in Fig. 9b. Moreover, we also built band-bending (Fig. 9a) for an ideal c-Si/a-B junction/diode based on the assumptions:

1. The charged interface is described by (c-)Si^{+q}/(a-)B^{-q} with the values for q given in the previous section.
2. The Fermi level of a-B is higher than that of c-Si as discussed at the beginning of Section III.
3. The Fermi level for Si atoms away from the interface is near the top of the valence band which bends upwards and part of this band becomes unoccupied.
4. Amorphous B away from the interfaces is a 'bad' metal with localized defect states. Therefore, its Fermi level will be changed nearby the interface due to filling of the defect states by extra electrons from Si.

The simulated c-Si/a-B interfaces contain not B doping. Thus, the junction is not a p-n type as believed before [3]. Figs. 2 and 4 showed that the a-B atoms near the Si substrates are of certain content of ordering with layering along the direction perpendicular to the substrates.

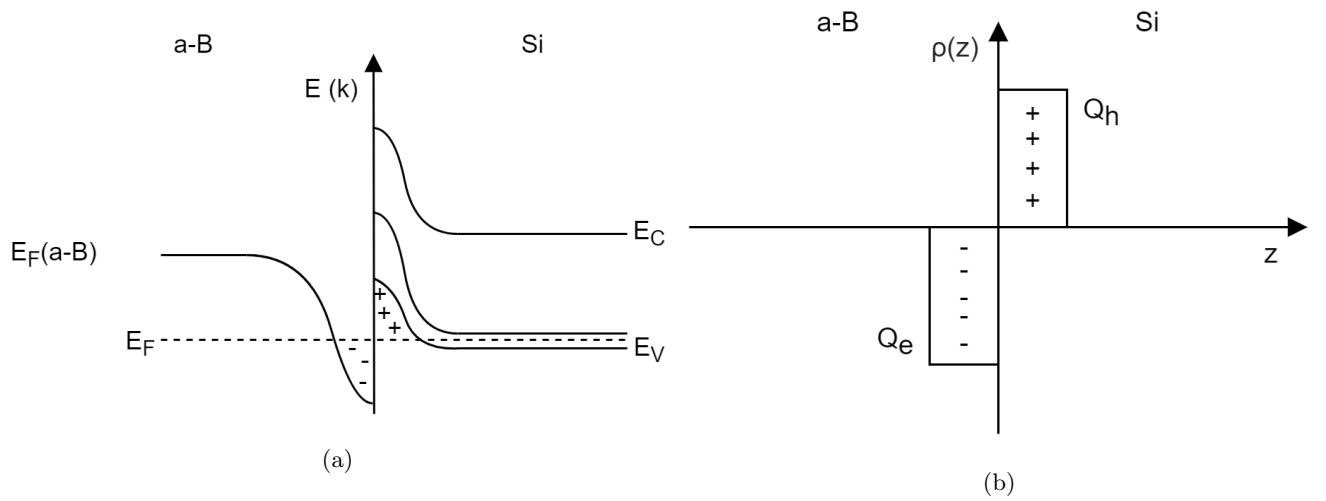

Figure 9: A schematic drawing of (a) band bending and (b) charge transfer at an ideal Si/a-B interface.

The densities of states of the a-B atoms near the substrates are rather low (Figs. 5 and 6) and the states at the Si band gap are localized as shown in Figs. 5 and 7. This indicates that though the a-B adjacent to the Si substrates are no semiconducting, the related electron states are localized. The a-B atoms adjacent to the substrate are 'bad' metals. This c-Si/a-B junction fits not in the category of Schottky-type as well. It could not be assigned to any existing type of heterojunctions. The rectification originates from the electric field induced in the regions near by the interface by the Si^+/B^- dipoles.

This model can be applied to the present c-Si/a-B devices with a-B deposited on a n-type silicon wafer [1–5, 13]. The strong electric fields across the c-(n-Si)/a-B interface caused by the interfacial charge transfer is responsible for the creation of a depletion zone in the n-silicon. As shown in [7], the formation of a deplete region reduces the charge at the interfacial Si atoms/ions just slightly. The electric field in the depletion zone and the related negative electric field at the nearby a-B region together define the rectifying properties of the diode.

V. CONCLUSION

Ab initio molecular dynamics simulations were performed for the Si{0 0 1}/a-B and Si{1 1 1}/a-B interfaces. The simulations revealed the formation of sharp c-Si/a-B interfaces which are chemically bonded. Each interfacial Si atom has predominantly two Si-B bonds for Si{0 0 1}/a-B and one Si-B bond for Si{1 1 1}/a-B.

Band structure calculations and charge analysis reveal charge transfer occurring from the interfacial Si to nearby B atoms with $\Delta q = 0.75$ e/Si (5.1×10^{18} e/m^2) for Si{0 0 1}/a-B and 0.40 e/Si (2.7×10^{18} e/m^2) for Si{1 1 1}/a-B, forming a pair of oppositely charged plates. This originates from the electronegativity differences between Si and B. The induced electric fields in the nearby regions by the Si^+/B^- dipoles rectify the charge-carrier flow. We also built band diagrams for a pure c-Si/a-B diode accordingly. The obtained information here is not only useful to get insight into the mechanism of the c-Si/a-B junctions/diodes, but also for further developments of new heterojunctions/diodes.

[1] F. Sarubbi, L. K. Nanver, T. L. M. Scholtes, and S. N. Nihtianov, Extremely Ultra -Shallow p^+-n Boron-Deposited Silicon Diodes Applied to DUV Photodiodes, in *2008 Device Research Conference* (IEEE, 2008).

[2] F. Sarubbi, L. K. Nanver, and L. M. Scholters, High Effective Gummel Number of CVD Boron Layers in Ultrashallow p^+n Diode Configurations, IEEE Trans. Electron Devices **57**, 1269 (2010).

[3] L. Shi, F. Sarubbi, L. K. Nanver, U. Kroth, A. Gottwald, and S. Nihtianov, Optical performance of B-layer ultrashallow-junction silicon photodiodes in the VUV spectral range, Procedia Eng. **5**, 633 (2010).

[4] S. Nihtianov, A. J. van der Sijs, P. W. J. Kemper, G. W. P. Baas, L. K. Nanver, F. Sarubbi, A. A. J. Schuwer, G. M. Gommeren, M. Pot, and T. L. M. Scholtes, RADIATION DETECTOR, METHOD OF MANUFACTURING A RADIATION DETECTOR, AND LITHOGRAPHIC APPARATUS COMPRISING A RADIATION DETECTOR (2013).

[5] T. Knezevic, X. Liu, E. Hardeveld, T. Suligoj, and L. K. Nanver, Limits on Thinning of Boron Layers With/Without Metal Contacting in PureB Si (Photo)Diodes, IEEE Electron Device Letters **40**, 858 (2019).

[6] C. M. Fang, V. Mohammadi, S. Nihtianov, and M. H. F. Sluiter, Stability, local structure and electronic properties of borane radicals on the Si(100) 2×1:H surface: A first-principles study, Computational Materials Science **140**,

253 (2017).
[7] V. Mohammadi, S. Nihtianov, and C. Fang, A dopingless junction-formation mechanism between n-silicon and an atomically thin boron layer, Scientific Reports **7**, 10.1038/s41598-017-13100-0 (2017).
[8] T. Kondo, Recent progress in boron nanomaterials, Science and Technology of Advanced Materials **18**, 780 (2017).
[9] C. Fang, V. Mohammodi, S. Nihtianov, and M. Sluiter, Stability, geometry and electronic properties of BH_n (n = 0 to 3) radicals on the Si{0 0 1}3 × 1:H surface from first-principles, Journal of Physics: Condensed Matter 10.1088/1361-648x/ab6e43 (2020).
[10] C. Kittel, *Introduction to Solid State Physics*, 8th ed. (Wiley, 2004).
[11] J. Singh, in *Semiconductor Devices* (Wiley, 2000) Chap. 7.
[12] R. T. Tung, The physics and chemistry of the Schottky barrier height, Applied Phys. Rev. **1**, 011304 (2014).
[13] L. K. Nanver, L. Qi, V. Mohammadi, K. R. M. Mok, W. B. de Boer, N. Golshani, A. Sammak, T. L. M. Scholtes, A. Gottwald, U. Kroth, and F. Scholze, Robust UV/VUV/EUV PureB photodiode detector technology with high CMOS compatibility, IEEE Journal of Selected Topics in Quantum Electronics **20**, 306 (2014).
[14] V. Mohammadi, W. B. De Boer, and L. K. Nanver, An analytical kinetic model for chemical-vapor deposition of pureB layers from diborane, J. Appl. Phys. **112**, 113501 (2012).
[15] M. Krakers, T. Kneevic, and L. K. Nanver, Reverse breakdown and light-emission patterns studied in Si PureB SPADs, in *2019 42nd International Convention on Information and Communication Technology, Electronics and Microelectronics (MIPRO)* (IEEE, 2019).
[16] T. Knezevic, T. Suligoj, X. Liu, L. K. Nanver, A. Elsayed, J. F. Dick, and J. Schulze, Back-end-of-line CMOS-compatible diode fabrication with pure boron deposition down to 50 ° C, in *ESSDERC 2019 - 49th European Solid-State Device Research Conference (ESSDERC)* (IEEE, 2019).
[17] L. K. Nanver, An experimental view on PureB silicon photodiode device physics, in *2018 41st International Convention on Information and Communication Technology, Electronics and Microelectronics (MIPRO)* (IEEE, 2018).
[18] F. Sarubbi, L. K. Nanver, and T. L. Scholtes, CVD delta-doped boron surface layers for ultra-shallow junction formation, ECS Trans. **3**, 35 (2006).
[19] R. Nojdelov and S. Nihtianov, Response Time of Detectors Based on a Boron-Silicon Junction, in *2018 IEEE SENSORS* (IEEE, 2018).
[20] F. Zheng, H. H. Pham, and L.-W. Wang, Effects of the c-Si/a-SiO_2 interfacial atomic structure on its band alignment: an *ab initio* study, Physical Chemistry Chemical Physics **19**, 32617 (2017).
[21] M. Lamers, L. E. Hintzsche, K. T. Butler, P. E. Vullum, C.-M. Fang, M. Marsman, G. Jordan, J. H. Harding, G. Kresse, and A. Weeber, The interface of a-SiN_x:H and Si: Linking the nano-scale structure to passivation quality, Solar Energy Materials and Solar Cells **120**, 311 (2014).
[22] L. Hintzsche, C. Fang, M. Marsman, M. Lamers, A. Weeber, and G. Kresse, Formation of a positive fixed charge at c-Si(111)/a-$Si_3N_{3.5}$:H Interfaces, Physical Review Applied **3**, 10.1103/physrevapplied.3.064005 (2015).
[23] T. A. Pham, T. Li, H.-V. Nguyen, S. Shankar, F. Gygi, and G. Galli, Band offsets and dielectric properties of the amorphous Si_3N_4/Si(100) interface: A first-principles study, Applied Physics Letters **102**, 241603 (2013).
[24] W. I. Choi, K. Kim, and S. Narumanchi, Thermal conductance at atomically clean and disordered silicon/aluminum interfaces: A molecular dynamics simulation study, Journal of Applied Physics **112**, 054305 (2012).
[25] E. U. Davanzo, *Aluminum-Silicon Contact Formation Through Narrow Dielectric Openings : Application To Industrial High Efficiency Rear Passivated Solar Cells*, Ph.D. thesis, Universität Konstanz, Konstanz (2012).
[26] K. Sato and Y. Kubota, *Ab Initio* Molecular Orbital Study on Acceleration Mechanism of Silane Plasma Chemical Vapor Deposition by Diborane, Applied Physics Express **4**, 056202 (2011).
[27] K. Sato, N. Kanda, T. Ogata, and Y. Kumashiro, Structures of the main precursors and initial decomposition products of diborane chemical vapor deposition: an experimental and *ab initio* molecular orbital study, Chemical Physics Letters **325**, 453 (2000).
[28] H. Watanabe, N. Yamada, and M. Okaji, Linear Thermal Expansion Coefficient of Silicon from 293 to 1000 K, International Journal of Thermophysics **25**, 221 (2004).
[29] K. A. Cherednichenko and V. L. Solozhenko, Thermal expansion of α-boron and some boron-rich pnictides, Solid State Communications **303-304**, 113735 (2019).
[30] L. E. Hintzsche, C. M. Fang, T. Watts, M. Marsman, G. Jordan, M. W. P. E. Lamers, A. W. Weeber, and G. Kresse, Density functional theory study of the structural and electronic properties of amorphous silicon nitrides: Si_3N_{4-x}:H, Phys. Rev. B **86**, 235204 (2012).
[31] C. M. Fang, H. Men, and Z. Fan, Effect of Substrate Chemistry on Prenucleation, Metallurgical and Materials Transactions A **49**, 6231 (2018).
[32] G. Kresse and J. Hafner, *Ab initio* molecular-dynamics simulation of the liquid-metal–amorphous-semiconductor transition in germanium, Phys. Rev. B **49**, 14251 (1994).
[33] G. Kresse and J. Furthmüller, Efficiency of ab-initio total energy calculations for metals and semiconductors using a plane-wave basis set, Computational Materials Science **6**, 15 (1996).
[34] P. E. Blöchl, Projector augmented-wave method, Phys. Rev. B **50**, 17953 (1994).
[35] G. Kresse and D. Joubert, From ultrasoft pseudopotentials to the projector augmented-wave method, Phys. Rev. B **59**, 1758 (1999).
[36] J. P. Perdew, K. Burke, and M. Ernzerhof, Generalized Gradient Approximation Made Simple, Phys. Rev. Lett. **77**, 3865 (1996).
[37] H. J. Monkhorst and J. D. Pack, Special points for Brillouin-zone integrations, Phys. Rev. B **13**, 5188 (1976).
[38] A. Pasquarello, M. S. Hybertsen, and R. Car, Interface structure between silicon and its oxide by first-principles molecular dynamics, Nature **396**, 58 (1998).
[39] W. Bludau, A. Onton, and W. Heinke, Temperature dependence of the band gap of silicon, Journal of Applied Physics **45**, 1846 (1974).
[40] F. H. Horn, Some Electrical and Optical Properties of Simple Rhombohedral Boron, Journal of Applied Physics **30**, 1611 (1959).

[41] R. O. Jones, Density functional theory: Its origins, rise to prominence, and future, Rev. Mod. Phys. **87**, 897 (2015).

[42] I. D. Brown, Recent Developments in the Methods and Applications of the Bond Valence Model, Chemical Reviews **109**, 6858 (2009).

[43] L. Pauling, The Nature of the Chemical Bond (Cornell University Press, 1960) pp. 111–120.

[44] N. Saitoh, T. Akamine, K. Aoki, and Y. Kojima, Composition and Growth Mechanisms of a Boron Layer Formed Using the Molecular Layer Doping Process, Japanese Journal of Applied Physics **32**, 4404 (1993).

[45] C. Fang and Z. Fan, Atomic ordering at the interfaces between liquid Al and solid MgO: An *Ab Initio* molecular dynamics study, Philosophical Magazine Letters **100**, 235 (2020).

[46] R. F. W. Bader, A Bond Path: A universal Indicator of Bonded Interactions, J. Phys. Chem. A **102**, 7314 (1998).

[47] G. Henkelman, A. Arnaldsson, and H. Jónsson, A fast and robust algorithm for Bader decomposition of charge density, Computational Materials Science **36**, 354 (2006).

[48] C. M. Fang, A. van Blaaderen, and M. A. van Huis, Stability and geometry of silica nano-ribbons (SNRs): a first-principles study, Physical Chemistry Chemical Physics **18**, 21825 (2016).

[49] P. Lorrain, D. R. Corson, and F. Lorrain, *Electromagnetic fields and waves : including electric circuits* (Freeman, New York, 1988).

[50] C. Fang, M. A. van Huis, D. Vanmaekelbergh, and H. W. Zandbergen, Energetics of polar and nonpolar facets of PbSe nanocrystals from theory and experiment, ACS Nano **4**, 211 (2009).

[51] G. A. Slack, C. I. Hejna, M. F. Garbauskas, and J. S. Kasper, The crystal structure and density of β-rhombohedral boron, Journal of Solid State Chemistry **76**, 52 (1988).

[52] E. D. Jemmis and M. M. Balakrishnarajan, Polyhedral Boranes and Elemental Boron: Direct Structural Relations and Diverse Electronic Requirements, Journal of the American Chemical Society **123**, 4324 (2001).

[53] M. J. van Setten, M. A. Uijttewaal, G. A. de Wijs, and R. A. de Groot, Thermodynamic Stability of Boron: The Role of Defects and Zero Point Motion, Journal of the American Chemical Society **129**, 2458 (2007).

[54] M. Kobayashi, Structure of amorphous boron, Journal of Materials Science **23**, 4392 (1988).

[55] M. Kobayashi, I. Higashi, and M. Takami, Fundamental Structure of Amorphous Boron, Journal of Solid State Chemistry **133**, 211 (1997).

[56] K. Jarolimek, R. A. de Groot, G. A. de Wijs, and M. Zeman, First-principles study of hydrogenated amorphous silicon, Physical Review B **79**, 10.1103/physrevb.79.155206 (2009).

[57] T. Knezevic, T. Suligoj, and L. K. Nanver, Impact of ultra-thin-layer material parameters on the suppression of carrier injection in rectifying junctions formed by interfacial charge layers, in *2019 42nd International Convention on Information and Communication Technology, Electronics and Microelectronics (MIPRO)* (IEEE, 2019).

[58] Y. Kumashiro, T. Yokoyama, J. Nakahura, K. Hatsuda, H. Yoshida, and J. Takahashi, Thermoelectric Properties of Boron and Boron Phosphide Film, MRS Proceedings **242**, 10.1557/proc-242-629 (1992).

[59] U. Kuhlmann, H. Werheit, T. Lundström, and W. Robers, Optical properties of amorphous boron, Journal of Physics and Chemistry of Solids **55**, 579 (1994).

[60] A. Hori, M. Takeda, H. Yamashita, and K. Kimura, Absorption Edge Spectra of Boron-Rich Amorphous Films Constructed with Icosahedral Cluster, Journal of the Physical Society of Japan **64**, 3496 (1995).

[61] K. Kumashiro, K. Hirata, K. Sato, T. Yokoyama, T. Aisu, T. Ikeda, and M. Minaguchi, Thermoelectric Properties of Boron and Boron Phosphide Films, Journal of Solid State Chemistry **154**, 26 (2000).

[62] O. A. Golikova, Amorphous boron films with enhanced electrical conductivity, Semiconductors **34**, 363 (2000).

[63] J. P. Schaffer, H. Park, J. H. Lind, and P. L. Jones, Hydrogenated amorphous boron: Transient and steady state photoconductivity, Physica Status Solidi A, Applied Research (1984).

[64] F. H. Cocks, P. L. Jones, and L. J. Dimmey, The optical band gap of hydrogenated amorphous-boron thin films: The effect of thermal treatment, Applied Physics Letters **36**, 970 (1980).

[65] M. Durandurdu, Amorphous boron suboxide, Journal of the American Ceramic Society **102**, 4546 (2019).

[66] L. E. Hintzsche, C. M. Fang, M. Marsman, G. Jordan, M. W. P. E. Lamers, A. W. Weeber, and G. Kresse, Defects and defect healing in amorphous $Si_3N_{4-x}H_y$: An *ab initio* density functional theory study, Physical Review B **88**, 10.1103/physrevb.88.155204 (2013).